Accepted Manuscript Online: 14 November 2016	Terr. Atmos. Ocean. Sci.	doi: 10.3319/TAO.2016.10.07.01

Accepted Manuscript

A strong-motion hot spot of the 2016 Meinong, Taiwan, earthquake (Mw=6.4)

Hiroo Kanamori[1, *], Lingling Ye[1], Bor-Shouh Huang[2], Hsin-Hua Huang[1,6], Shiann-Jong Lee[2], Wen-Tzong Liang[2], Yen-Yu Lin[1,2], Kuo-Fong Ma[3], Yih-Min Wu[4,5], and Te-Yang Yeh[2]

[1] Seismological Laboratory, California Institute of Technology, Pasadena, Calfornia, USA

[2] Institute of Earth Sciences, Academia Sinica, Taipei, Taiwan

[3] Department of Earth Sciences, National Central University, Taoyuan, Taiwan

[4] Department of Geosciences, National Taiwan University, Taipei, Taiwan

[5] National Center for Research on Earthquake Engineering, NARLabs, Taipei, Taiwan

[6] Department of Geology and Geophysics, University of Utah, Salt Lake City, UT

Received 25 July 2016, revised 6 October 2016, accepted 7 October 2016

DOI: 10.3319/TAO.2016.10.07.01

*Corresponding author: hiroo@gps.caltech.edu

A strong-motion hot spot of the 2016 Meinong, Taiwan, earthquake (Mw=6.4)

Hiroo Kanamori[1], Lingling Ye[1], Bor-Shouh Huang[2], Hsin-Hua Huang[1,6], Shiann-Jong Lee[2], Wen-Tzong Liang[2], Yen-Yu Lin[1,2], Kuo-Fong Ma[3], Yih-Min Wu[4,5], and Te-Yang Yeh[2]

[1] *Seismological Laboratory, California Institute of Technology, Pasadena, Calfornia, USA*

[2] *Institute of Earth Sciences, Academia Sinica, Taipei, Taiwan*

[3] *Department of Earth Sciences, National Central University, Taoyuan, Taiwan*

[4] *Department of Geosciences, National Taiwan University, Taipei, Taiwan*

[5] *National Center for Research on Earthquake Engineering, NARLabs, Taipei, Taiwan*

[6] *Department of Geology and Geophysics, University of Utah, Salt Lake City, UT 84112*

This manuscript is submitted to "Terrestrial, Atmospheric and Oceanic Sciences"

Running title: A strong-motion hot spot of the 2016 Meinong earthquake

Key Points:

1) Large ground-motion amplification occurred near Tainan during the Meinong event.
2) Amplification is due to radiation pattern, site effect, and directivity.
3) Moderate earthquakes can cause damaging ground motions if such combination occurs.

Corresponding author: Hiroo Kanamori, Seismological Laboratory, California Institute of Technology, Pasadena, California 91125, hiroo@gps.caltech.edu, (626) 395-6914, FAX: (626) 564-0715

Abstract

Despite a moderate magnitude, Mw=6.4, the 02/05/2016 Meinong, Taiwan, earthquake caused significant damage in Tainan City and the surrounding areas. Several seismograms display an impulsive S-wave velocity pulse with an amplitude of about 1 m/s, which is similar to large S-wave pulses recorded for the past several larger damaging earthquakes, such as the 1995 Kobe, Japan, earthquake (Mw=6.9) and the 1994 Northridge, California, earthquake (Mw=6.7). The observed PGV in the Tainan area is about 10 times larger than the median PGV of Mw=6.4 crustal earthquakes in Taiwan. We investigate the cause of the localized strong ground motions. The peak-to-peak ground-motion displacement at the basin sites near Tainan is about 35 times larger than that at a mountain site with a similar epicentral distance. At some frequency bands (0.9 to 1.1 Hz), the amplitude ratio is as large as 200. Using the focal mechanism of this earthquake, typical "soft" and "hard" crustal structures, and directivity inferred from the observed waveforms and the slip distribution, we show that the combined effect yields an amplitude ratio of 17 to 34. The larger amplitude ratios at higher frequency bands can be probably due to the effects of complex 3-D basin structures. The result indicates that even from a moderate event, if these effects simultaneously work together toward amplifying ground motions, the extremely large ground motions as observed in Tainan can occur. Such occurrences should be taken into consideration in hazard mitigation measures in the place with frequent moderate earthquakes.

Keywords: 2016 Meinong earthquake, Directivity, Site response, S-wave pulse

1. Introduction

The February 5, 2016 Meinong earthquake (U.S. Geological Survey hypocenter parameters: 19:57:27 UTC, Mw=6.4, 22.94°N; 120.60°E, 23.0 km) which occurred near the City of Tainan, Taiwan, caused severe damage with 117 fatalities and collapse of tall buildings despite its moderate magnitude (Figure 1a). It is the most damaging earthquake in Taiwan since the 1999 Mw=7.6 Chi-Chi earthquake. The peak local intensity reported by the Central Weather Bureau (CWB) of Taiwan was 7, the highest on the Taiwan intensity scale with PGA > 400 cm/s^2. A concise summary of the tectonic framework of this earthquake is given by Huang et al. (2016).

Immediately after the occurrence of the event, the waveforms of local ground motions recorded with the Taiwan Early Warning System Palert (Wu et al., 2013) were released. The Palert records used in this study are available to the public (Wu et al., 2016) and can be downloaded from the cloud disk at the National Taiwan University (https://www.space.ntu.edu.tw/navigate/s/5CDFA7C2CFD7487FB84E2CE3F7376C33QQY). To our surprise, the record from the station W21B, about 27 km WNW (φ (azimuth)=299°) from the epicenter, displayed an impulsive velocity pulse with an amplitude of about 1m/s (Figure 1b). As shown in Figure 2, the W21B velocity pulse is comparable to the velocity pulses recorded for several damaging earthquakes in the past, especially the one recorded at the Olive View Hospital during the 1994 Northridge, California, earthquake. Hall et al. (1995) and Heaton et al. (1995) emphasized the engineering implications of these large velocity pulses especially for the safety of tall buildings. As will be shown later, the records at a few other stations, like TAI1 (CHY078) and CHN3 (CHY089) (locations are shown in Figure 1a) near W21B display equally impulsive large velocity pulses. Also shown in Figure 1 is the location of station MASB which will be used

as a reference bedrock site. We will compare the ground motions at soft basin sites to those at this bedrock station.

This study is motivated by these unusual observations, and discusses the hazard implications of ground motions from moderate earthquakes in urban environments.

2. Overall source characteristics of the 2016 Meinong earthquake

Although our main objective is to understand the cause of the unusually strong ground motions, rather than to perform detailed analyses of the rupture mechanism of this particular earthquake, we first investigate the overall source characteristics of this earthquake over a broad frequency band. A good source model is a prerequisite for understanding the excitation of seismic waves which ultimately determines the nature of ground motions.

2.1 W phase inversion

Since the crustal structure of Taiwan is complex, varying rapidly from thick basin structures on the west coast to bed-rock sites in the central mountains, propagation of short period waves is complex. To avoid the complex propagation effects, we first study long-period W phases recorded with the Taiwan BATS network (Institute of Earth Sciences (1996); bats.earth.sinica.edu.tw) and determine the long-period characteristics up to a period of 150 s. The method is described in Kanamori and Rivera (2008), but for applications to moderate regional events, we use a structure shown in Table 1, and a higher frequency band 0.0067 Hz (150 s) to 0.02 Hz (50 s) than the standard frequency band (0.001 Hz (1000 s) to 0.005 Hz (200 s)). Figure 3 shows the result. The best double-couple solution is given by strike/dip/rake (s/d/r)=295°/30°/37° and 172°/73°/115° and is similar to those obtained by various investigators using different methods, different data sets, and different frequency bands (e.g., Huang et al. (2016), Lee et al. (2016), also http://tesis.earth.sinica.edu.tw/showDetail.php?date=%272016-02-06%27&time=%2703:57:27%27).

Thus, despite the extreme lateral heterogeneity of the structure, the geometry of the source appears to be well constrained at long period. The nearest stations MASB to the south is shown in Figure 1a, Δ (distance)=34km, φ (azimuth) =165°).

2.2 Teleseismic body-wave inversion

We next investigate teleseismic P and SH waves over a period range from 2 to 30 s. Figure 4 summarizes the result of teleseismic body-wave inversion. The method used is similar to that described in Hartzell and Heaton (1983), and the code used is based on the one archived at http://wwweic.eri.u-tokyo.ac.jp/ETAL/KIKUCHI but with extensive modifications and additions made at the University of California, Santa Cruz, described in Ye et al. (2016).

The crustal structure used for inversion is shown in Table 2. We used the mechanism s/d/r=281°/24°/23.8° given by the initial solution of the Global Centroid Moment Tensor (GCMT) Project, and the rupture speed used for inversion shown in Figure 4 is 3 km/s. We obtain a seismic moment of M_0=5.05 x10^{18} Nm (Mw=6.4). Figure 4a shows the moment-rate function viewed from large distance normal to the fault plane. This should be regarded as an "average" moment rate function. As will be shown later, the moment-rate function viewed from different azimuths varies depending on directivity. Although the total duration of the source is about 17 sec, the main pulse is only about 5 sec long. The red curve on Figure 4b shows the moment-rate spectrum at frequencies higher than 0.05 Hz estimated from the observed displacement records. The dashed curve in Figure 4b is the reference omega-squared moment-rate spectrum computed with a stress parameter of 3MPa (see Ye et al., 2016). We compute the radiated energy E_R from the observed spectrum (red curve) as E_R=2.81x10^{14} J with a scaled energy E_R/M_0=5.56x10^{-5}. Figure 4c shows the P and SH radiation patterns. Figure 4d shows the

slip distribution on the fault dipping 24° to the north. The NS trending steep nodal plane could be used as the fault plane but the north dipping plane can explain the directivity better. From the waveform inversion alone, we cannot determine which of the 2 nodal panes is the fault plane. The analyses by Huang et al. (2016) and Lee et al. (2016) suggest that the static horizontal displacement field appears to favor the north-dipping nodal plane as the fault plane. The rake angle and the slip function are shown on each 4x4 km^2 subfault. Note that the local slip function is very short, 0.5 to 1 s, on most subfaults. This slip distribution is in general similar to that obtained by Lee et al. (2016) in which local and global seismic data and geodetic data were jointly used. Figure 4e shows the distribution of stress drop with the average of about 1 MPa, but the absolute value depends on the assumed rupture speed. If we use a rupture speed of 2.5 and 3.5 km/s, the stress drop is 1.7 and 0.6 MPa, respectively. Figure 4f compares the observed and synthetic teleseismic P and SH waveforms showing overall good agreement. Although teleseismic data do not have enough resolution to determine the detailed slip distribution for a small to moderate event like this, the recent high-quality broadband waveforms at many stations as shown in Figure 4f contain important information of the event. We include these waveforms here because they are often useful for checking some details of the source characteristics.

3. Interpretation of large ground motions

To interpret the details of ground motions, ideally we should invert all the regional and teleseismic data together using a detailed three-dimensional (3-D) structure in Taiwan. Although extensive studies have been made in Taiwan to determine 3-D crustal structures, given the extreme lateral variations of the site response near the epicentral area and the relatively short period waves involved, a complete 3-D inversion study is not practical. Here, we take a simpler

approach by examining each important ground-motion record after having determined the overall gross source characteristics as shown in Figures 3 and 4. Our objective is to understand why such localized strong ground motions were produced by this earthquake, rather than to explain every detail of the observed records. Since the events in the future are unlikely to occur in exactly the same way as the events in the past, we believe that a good understanding of the special circumstance which caused the observed strong-motion hot spot is critically important for implementing comprehensive hazard mitigation measures in the future.

3.1 Comparison of the records at stations W21B and MASB

To investigate approximate spatial variability of ground motions, first we compare the ground motions at W21B and MASB (Figure 5). These stations are among the closest stations with very different ground-motion periods and amplitudes. As shown in Figure 5, the pulse width is 2.7 s at W21B while it is 5.5 s at MASB. The peak-to-peak amplitude at W21B (EW component) is approximately 35 times larger than that at MASB (EW component). The azimuthal amplitude variation of this magnitude has been seldom observed. The factor of 35 is the amplitude ratio of the whole trace. If we compare the amplitude ratio at different frequency bands, the amplification factors are 35, 160, 120, 140, and 210 for the frequency bands 0.1 to 0.3 Hz, 0.3 to 0.5 Hz, 0.5 to 0.7 Hz, 0.7 to 0.9 Hz, and 0.9 to 1.1 Hz, respectively (Figure 6). The observed large displacement amplitude ratios are also reflected in PGA (ratio= $\frac{450\ \mathrm{cm/s^2\,(W21B\_E)}}{10.9\ \mathrm{cm/s^2\,(MASB\_E)}}$=41), PGV (ratio= $\frac{100\ \mathrm{cm/s\ (W21B\_E)}}{0.9\ \mathrm{cm/s\ \ (MASB\_E)}}$=111) and in the spectral acceleration and spectral velocity as shown in Figure 7; the ratio of spectral amplitude at the period of 1 to 2 s is $\frac{\mathrm{W21B\_E}}{\mathrm{MASB\_E}} = 150\,\mathrm{to}\,160$.

Note that these ratios are the amplitude ratios of W21B to MASB, and not the amplification factor at W21B. According to Liu and Tsai (2005), the median values of PGA and PGV of Mw=6.4 crustal earthquakes in Taiwan are approximately 100 cm/s^2, and 9 cm/s, respectively (figures 3 and 4 of Liu and Tsai, 2005). Thus, these observations mean that PGA and PGV at W21B are, respectively, about 4.5 and 10 times larger than the median value for Taiwan crustal earthquakes.

3.2 Factors that control the ground-motion amplitude

We now examine why the amplitude is so different between W21A and MASB by considering three factors: 1) geometrical effect of the radiation pattern; 2) site and propagation effect; and 3) directivity.

Crustal structure

To make these comparisons, we need to know the crustal structures for this area. Since we do not have a specific model for this area, we characterize the structures by a "hard" and "soft" model shown in Table 3 and Figure 8. Several crustal models have been presented for Taiwan (e.g., Hwang et al., 2003; Huang et al., 2013; Kuo et al., 2015; Lin et al., 2009; Wu and Huang, 2013; Huang et al., 2014). To represent the soft basin structure for the station W21B, we refer to the S wave structure in the shallow crust shown in Lin et al. (2009) for a profile near Jiali (Lat. 23.17°N, Long. 120.17°E). We construct a structure for a "soft" path by combining the shallow structure given by Lin et al. (2009) with a structure for a deeper crust taken from Huang et al. (2014). For the "hard" path, we simply remove the top 5 soft layers (layer 4 and layer 5 are identical) from the structure for the "soft" path. The structures shown in Table 3 and Figure 8 are constructed this way. We do not attempt to model the exact propagation effect, and our objective is to assess the effect of typical crustal structures on propagation of the waves along the strikingly different structures.

Radiation pattern effect

The effect of the radiation pattern on the amplitude can be determined by comparing the amplitude of synthetic seismograms computed for the stations W21B and MASB using the same

structure “hard” and “soft” structures. As shown in Figure 9, the amplitude ratio W21B/MASB is about 3 to 4 either for hard or soft structure. This ratio is for the peak-to-peak trace amplitude of the impulsive S-wave pulse and just an approximate value.

Site effect

Here the site effect is not the strict site response used in engineering practice; it is the amplitude ratio of the synthetics computed for a 1-D “soft” and “hard” structure shown in Figure 8. We do not include 3-D site response effects here. From Figure 9, the peak-to-peak amplitude ratio of “soft” to “hard” case is about 5 for W21B and 3.5 for MASB.

For comparison, Figure 10 shows the crustal response functions (the ratio of [amplitude at the surface]/[amplitude of incoming plane wave at the base]) (Haskell, 1962) for a vertically incident SH wave for the “soft” and “hard” crust. The ratio of the response function is on the average consistent with the ratio of the trace amplitude shown in Figure 9.

Directivity

The difference of the pulse width observed at W21B (2.7s) and MASB (5.5 s) clearly suggests significant directivity toward W21B (azimuth 299°) (i.e., toward north-west and down-dip). The pulse width ratio of 2 suggests that the amplitude ratio due to directivity is 1/2. The slip inversion of teleseismic data shown in Figure 4 does not have sufficient resolution to accurately determine the rupture directivity. However, as shown in Figures 4 and 11, even with the limited resolution, the rupture appears to have propagated mainly to the north from the hypocenter with a slight westward component. Since the slip near the hypocenter is small, the main pulse must be produced by a large slip patch about 10 km to the north of the hypocenter.

Figure 11 shows the moment rate functions as viewed from various azimuths. The moment-rate function viewed from the station W21B (red) is significantly shorter than that from the station MASB (blue), which is qualitatively consistent with the observation shown in Figures 5 and 11. However, a counter-clockwise rotation of the slip pattern by 30° would make the agreement with the observation even better. Given the limited resolution of the teleseismic inversion, we consider the slip pattern is satisfactorily supportive of the observed directivity effect of about 2. For comparison, the waveforms at W21B and MASB are shown on the left side of the figure. The slip model derived from a data set including local seismic data by Lee et al. (2016) suggests stronger westward directivity.

Expected amplitude variation

If we combine the effects of the three factors, we get a range of amplification factor of 17 to 34 (radiation pattern (2.4 to 3.4) x path-site effect (3.5 to 5) x directivity (2)), which is comparable to the observed ratio 35. However, as shown by Figure 6, even larger ratios at high frequency bands suggest another factor caused by the 3-D basin structure near the stations around Tainan. Thus, we conclude that the very large ground motions observed near Tainan were a result of unfortunate combination of these factors. Although this may not occur frequently, it is important to realize that even a moderate earthquake can produce unexpectedly damaging ground motions if such a circumstance occurs. Lee et al. (2016) arrived at a similar conclusion on the basis of detailed inversion of seismic and geodetic data. Our conclusion is based on direct comparisons of the observed records.

4. Comparison of the observed and synthetic ground motions observed at some stations

As mentioned earlier, the station W21B is a Palert network station and the accelerograph is placed in a building, i.e., the record is not a standard free-field record. To investigate how representative the W21B ground motion is in the Tainan area, we compare in Figure 12 the W21B records with those at nearby CWB stations TAI1 and CHN3 (Figure 1). Although the amplitude at the station TAI1 is considerably smaller than that at W21B, the amplitude at CHN3 is comparable to that at W21B. The ground motion amplitude is strongly affected by the shallow structure with a very low S-wave speed, less than 0.6 km/s, and considerable spatial variations in amplitudes and waveforms are expected. Nevertheless, the comparable amplitudes at the stations W21B and CHN3 indicate that the large displacement and velocity amplitudes at W21B are not particularly anomalous, and can be regarded as approximate free-field values.

We compute seismograms for these stations and compare them with the observed waveforms. For this computation we use a frequency-wavenumber integration code developed by Herrmann (2013). The three-component displacement and velocity waveforms thus computed are shown in Figure 12 for comparison with the observed. For the stations W21B, TAI1, and CHN3, we used the "soft" structure shown in Figure 8. First, we compute an impulse response using a 0.3 s wide trapezoidal (0.1 s rise and fall-off times) source function using the mechanism s/d/r=288°/17°/26° (M_0=5x10^{18} Nm), and convolve it with a triangular function (unit area) with a total width of 1.0 s to match the approximate width of the observed displacement and velocity pulses.

Given our insufficient knowledge of the 3-D structures in the area, we do not attempt to explain the every detail of the ground motion. However, the observed ground motions are approximately what are expected for those produced by the combination of the effects of radiation pattern, site effects, and directivity which all contribute toward amplifying the ground motion to the level unexpected of a moderate earthquake.

At the station MASB, the EW component displays a clear displacement and velocity pulse. The peak-to-peak displacement amplitude is only 1.4 cm, and the pulse width is about 5.5 s (Figure 13d) in contrast to the 2.7 s wide pulse observed at W21B (EW component). This broad pulse can be explained well with the directivity as shown in Figure 13. Figure 13a is the computed displacement for MASB using the "hard" crust and an impulse source. Figure 13b is an assumed source function. Figure 13c is the convolution of a) and b) which compares well with the observed record shown in Figure 13d. The source function shown in Figure 13b is constructed such that the initial small and the later large motions correspond, respectively, to the small slip near the hypocenter and the large slip at the patch about 10 km to the north shown in Figures 4 and 11. The details are adjusted to match the observed waveform. Considering the expected moment-rate function viewed from the azimuth of MASB shown in Figure 11, the shape of the assumed source function (Figure 13b) is reasonable.

5. Conclusion

Although the short (1 to 1.5 s) impulsive S-wave velocity pulse observed near Tainan is surprising, we conclude that the radiation pattern, path-site effects, and directivity all worked together to produce the strong S pulse. Energy focusing and trapping due to a 3-D structure most likely have contributed to further enhancing the effects at high frequency. More definitive

confirmation would require detailed waveform studies using detailed 3-D structures. Lee et al. (2016) represents an important step toward this goal.

The result indicates that if these effects simultaneously work together toward amplifying ground motions, the extremely large ground motions as observed in Tainan can occur even for a moderate event. Such occurrences should be taken into consideration in hazard mitigation measures in the place with frequent moderate earthquakes like Taiwan.

Acknowledgments

The Data Management System of the Incorporated Research Institutions for Seismology (http://www.iris.edu/hq/) was used to access the seismic data from the Global Seismic Network and Federation of Digital Seismic Network stations. We thank Thorne Lay for providing us with useful suggestions on inversion of teleseismic data and Luis Rivera for helping us to use the Hermann's frequency-wavenumber integration code. We benefited from the discussion with The-Ru Alex Song in the early stage of this work. Part of this research was conducted while Hiroo Kanamori was visiting the Institute of Earth Sciences, Academia Sinica under the Distinguished Visiting Fellow program of Academia Sinica. We thank two anonymous reviewers for helpful comments.

REFERENCES

Hall, J. F., T. H. Heaton, M. W. Halling, and D. J. Wald (1995), Near-source ground motion and its effects on flexible buildings, *Earthquake Spectra*, *11*, 569-605.

Hartzell, S. H., and T. H. Heaton (1983), Inversion of strong ground motion and teleseismic waveform data for the fault rupture history of the 1979 Imperial Valley, California, earthquake, *Bulletin of the Seismological Society of America*, *73*(6A), 1553-1583.

Haskell, N. A. (1962), Crustal reflection of plane P and SV waves, *Journal of Geophysical Research*, *67*(12), 4751-4768, doi:10.1029/JZ067i012p04751.

Heaton, T. H., J. F. Hall, D. J. Wald, and M. W. Halling (1995), Response of High-Rise and Base-Isolated Buildings to a Hypothetical Mw 7.0 Blind Thrust Earthquake, *Science*, *267*(5195), 206-211, doi:10.1126/science.267.5195.206.

Herrmann, R. B. (2013), Computer Programs in Seismology: An Evolving Tool for Instruction and Research, *Seismological Research Letters*, *84*(6), 1081-1088, doi:10.1785/0220110096.

Huang, M.-H., H. Tung, E. Fielding, H.-H. Huang, C. Liang, C. Huang, and J.-C. Hu (2016), Multiple fault slip triggered above the 2016 Mw 6.4 MeiNong earthquake in Taiwan, *Geophys. Res. Lett.*, doi:10.1002/2016GL069351.

Huang, B. S., C. Y. Wang, D. Okaya, S. J. Lee, Y. C. Lai, F. T. Wu, W. T. Liang, and W. G. Huang (2013), Multiple Diving Waves and Steep Velocity Gradients in the Western Taiwan Coastal Plain: An Investigation Based on the TAIGER Experiment, *Bulletin of the Seismological Society of America*, *103*(2A), 925-935, doi:10.1785/0120110047.

Huang, H.-H., Y.-M. Wu, X. Song, C.-H. Chang, S.-J. Lee, T.-M. Chang, and H.-H. Hsieh (2014), Joint Vp and Vs tomography of Taiwan: Implications for subduction-collision orogeny, *Earth and Planetary Science Letters*, *392*, 177-191, doi:http://dx.doi.org/10.1016/j.epsl.2014.02.026.

Hwang, R.-D., G.-K. Yu, W.-Y. Chang, and J.-P. Chang (2003), Lateral variations of shallow shear-velocity structure in southwestern Taiwan inferred from short-period Rayleigh waves, *Earth, Planets and Space*, *55*(6), 349-354, doi:10.1186/bf03351768.

Institute of Earth Sciences, Academia Sinica, Taiwan (1996), Broadband Array in Taiwan for Seismology, doi:10.7914/SN/TW.

Kanamori, H., and L. Rivera (2008), Source inversion of W phase: speeding up seismic tsunami warning, *Geophysical Journal International*, *175*(1), 222-238, doi:10.1111/j.1365-246X.2008.03887.x.

Kuo, C.-H., K.-L. Wen, C.-M. Lin, S. Wen, and J.-Y. Huang (2015), Investigating near surface S-wave velocity properties using ambient noise in southwestern Taiwan, *Terr. Atmos. Ocean. Sci., 26*, 205-211, doi:10.3319/TAO.2014.12.02.05(EOSI).

Lee, S. -J., T.-Y. Yeh, and Y.-Y. Lin (2016), Anomalously large ground motion in the 2016 ML 6.6 Meinong, Taiwan, earthquake: A synergy effect of source rupture and site amplification, Seismol. Res. Lett., doi: 10.1785/0220160082.

Lin, C.-M., T.-M. Chang, Y.-C. Huang, H.-J. Chiang, C.-H. Kuo, and K.-L. Wen (2009), Shallow S-wave velocity structures in the western coastal plain of Taiwan, *Terr. Atmos. Ocean. Sci., 20*, 299-308, doi:10.3319/TAO.2007.12.10.01(T).

Liu, K.-S., and Y.-B. Tsai (2005), Attenuation Relationships of Peak Ground Acceleration and Velocity for Crustal Earthquakes in Taiwan, *Bulletin of the Seismological Society of America, 95*(3), 1045-1058, doi:10.1785/0120040162.

Wu, Y. M., D. Y. Chen, T. L. Lin, C. Y. Hsieh, T. L. Chin, W. Y. Chang, W. S. Li, and S. H. Ker (2013), A High-Density Seismic Network for Earthquake Early Warning in Taiwan Based on Low Cost Sensors, *Seismological Research Letters, 84*(6), 1048-1054, doi:10.1785/0220130085.

Wu, Y. M., W. T. Liang, H. Mittal, W. A. Chao, C. H. Lin, B. S. Huang, and C. M. Lin (2016), Performance of a low-cost earthquake early warning system (P-alert) during the 2016 ML 6.4 Meinong (Taiwan) earthquake, *Seismo. Res. Let.* **87**, 1050-1059, doi: 10.1785/0220160058.

Wu, C. F., and H. C. Huang (2013), Near-Surface Shear-Wave Velocity Structure of the Chiayi Area, Taiwan, *Bulletin of the Seismological Society of America, 103*(2A), 1154-1164, doi:10.1785/0120110245.

Ye, L., T. Lay, H. Kanamori, and L. Rivera (2016), Rupture characteristics of major and great (Mw $\geq$ 7.0) megathrust earthquakes from 1990 to 2015: 1. Source parameter scaling relationships, *Journal of Geophysical Research: Solid Earth*, *121*(2), 826-844, doi:10.1002/2015JB012426.

Table 1 Crustal structure used for W phase inversion. (H:thickness; α (P-wave speed; β:S-wave speed; ρ:density). Crust is underlain by a PREM-like mantle structure.

H(km)	α (km/s)	β (km/s)	ρ (g/cm^3)
18	6.0	3.5	2.6
15	6.7	3.8	3.38
7	7.7	4.3	3.38

Table 2. Crustal structure used for teleseismic inversion.

H(km)	α (km/s)	β (km/s)	ρ (g/cm^3)
0.7	2.5	1.2	2.1
14.3	6.0	3.5	2.7
9.0	6.6	3.7	2.9
11.0	7.2	4.0	3.05
half space	7.8	4.4	3.5

Table 3. Crustal structure used for modeling local wave-field. The structure shown is for the "soft" structure model, and the "hard" structure model is constructed by removing the top 5 layers.

Layer	H(km)	α (km/s)	β (km/s)	ρ (g/cm^3)	Q_α	Q_β
1	0.5	1.5	0.58	2.0	40	20
2	0.5	2.5	1.0	2.2	120	60
3	0.5	2.8	1.2	2.2	600	300
4	0.5	4.2	1.7	2.2	600	300
5	0.5	4.2	1.7	2.2	600	300
6	2.0	4.44	2.556	2.4	600	300
7	5.0	5.25	3.035	2.6	600	300
8	4.0	6.05	3.457	2.6	600	300
9	4.0	6.36	3.655	2.7	600	300
10	8.0	6.66	3.85	2.7	600	300
11	5.0	7.14	4.103	2.7	600	300
12	5.0	7.43	4.27	2.8	600	300
13	15.0	7.71	4.406	2.8	600	300
14	20.0	7.96	4.628	3.0	600	300
15	20.0	8.1	4.629	3.1	600	300
16	4.0	8.23	4.73	3.3	600	300

Figure Caption

Figure 1.

a) PGA distribution of the 2016 Meinong earthquake (circles: CWB stations; squares: Palert stations; triangles: BATS stations). The epicenter is indicated by a star, and the 4 stations discussed are indicated by their station names. b) The EW component ground-motion acceleration, velocity and displacement recorded at a Palert station W21B. The ground-motion waveforms recorded at station MASB are shown in Figures 5, 11, and 13.

Figure 2.

Ground-motion velocity recorded at W21B (EW component) for the 2016 Meinong earthquake compared with the S-wave pulses of damaging large earthquakes in the past (modified from Hall et al., 1995). Note the similarity of the waveforms between the 1994 Northridge earthquake and the 2016 Meinong earthquake.

Figure 3.

Inversion of W phases at the frequency band of 0.0067 Hz (150 s) to 0.02 Hz (50 s). The black and red curves show the observed and synthetic waveforms computed for the solution shown. The two red dots bracket the portion of the observed waveforms used for inversion.

Figure 4.

Inversion of teleseismic body waves. a) Moment-rate function and b) moment-rate spectrum. c) P and SH radiation patterns with the stations used for inversion. The mechanism is given by (slip/dip/rake=281°/24°/24°), d) Slip distribution, e) distribution of stress drop, and f) observed (black) and computed (red) teleseismic P and SH displacement and velocity

waveforms. For each station, the first row shows the displacement and the second row shows the velocity. A rupture speed of 3 km/s is assumed.

Figure 5.

Comparison of the EW component displacement waveforms at the stations W21B and MASB. On the plot for MASB, the black curve (marked as x1) is the plot with the same amplitude scale as that for W21B, and the gray curve (x40) shows the displacement multiplied by 40, indicating that the trace amplitude at W21B is about 35 times larger than that at MASB.

Figure 6.

Comparison of the amplitude at W21B (black) and at MASB (gray) at 5 frequency bands. For each frequency band the records are Butterworth band-pass filtered. For comparison, the MASB record is multiplied by a factor given at the lower left of each figure. Note that at the frequency band 0.3 to 0.5 Hz (2 to 3.3 s), the amplitude ratio is about 160.

Figure 7.

Spectral acceleration (a) and spectral velocity (b) computed for the records at MASB (EW component), W21B (EW component), CHN3 (NS component), and TAI1 (EW component). Damping is 5 %.

Figure 8.

S-wave vertical profile used for the “soft” structure model. The “hard structure model is obtained by removing the top 5 layers above the depth indicated by a dashed line.

Figure 9.

Synthetic displacement waveforms computed for the stations W21B and MASB using the "soft" and "hard" structure models.

Figure 10.

Crustal response functions for a vertically incident SH waves for the "soft" (gray curve) and "hard" (black curve) crustal structure models.

Figure 11.

The moment-rate functions (shaded pattern) viewed from various azimuths. The slip distribution is shown on the right. The stations W21B and MASB are located in the azimuth of 299° and 165. The moment-rate functions viewed from the azimuth of W21B and MASB are shown in red and blue, respectively. The displacement record at the respective station is shown for comparison.

Figure 12.

Comparison of the observed (top) and synthetic (bottom) waveforms for the station W21B (Figure 12a), TAI1 (Figure 12b), and CHN3 (Figure 12c). Three-component displacement and velocity waveforms are shown. The "soft" crustal structure model is used.

Figure 13.

Comparison of the observed and synthetic E-W component waveforms for the station MASB. The "hard" crustal structure model is used. a) Synthetic displacement waveform computed for a trapezoidal source function with a total duration of 0.3 s. b) The assumed moment-rate function. c) Convolution of a) and b). d) The observed displacement waveform.

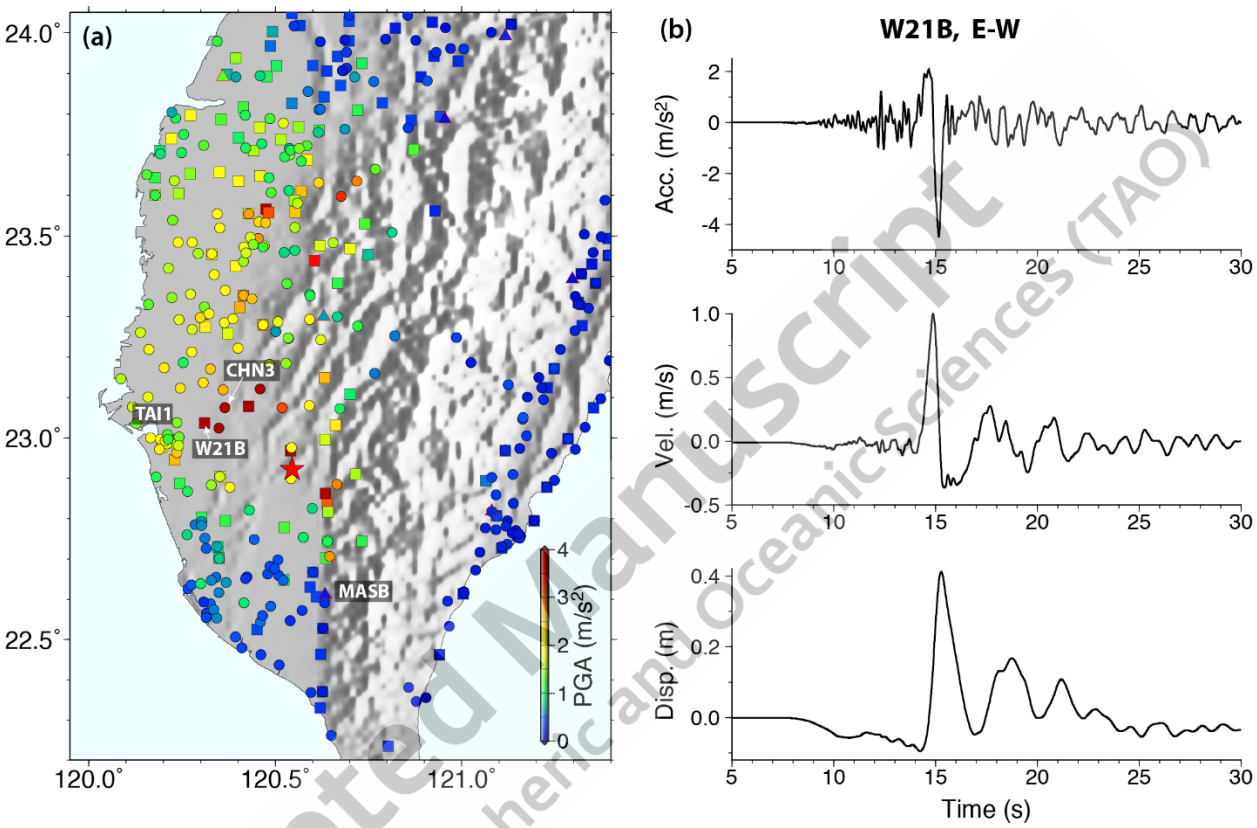

Figure 1.

a) PGA distribution of the 2016 Meinong earthquake (circles: CWB stations; squares: Palert stations; triangles: BATS stations). The epicenter is indicated by a star, and the 4 stations discussed are indicated by their station names. b) The EW component ground-motion acceleration, velocity and displacement recorded at a Palert station W21B. The ground-motion waveforms recorded at station MASB are shown in Figures 5, 11, and 13.

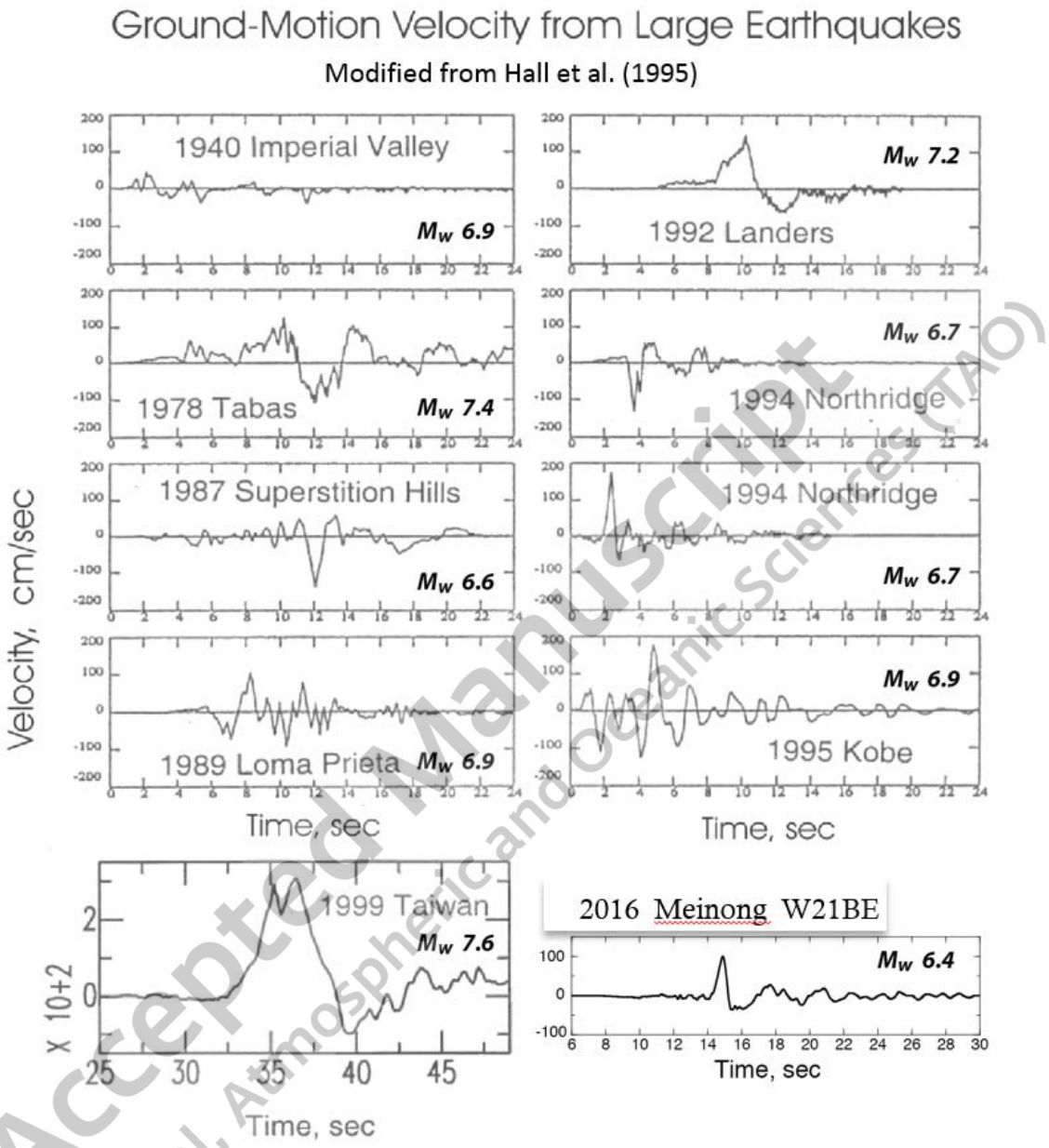

Figure 2.

Ground-motion velocity recorded at W21B (EW component) for the 2016 Meinong earthquake compared with the S-wave pulses of damaging large earthquakes in the past (modified from Hall et al., 1995). Note the similarity of the waveforms between the 1994 Northridge earthquake and the 2016 Meinong earthquak

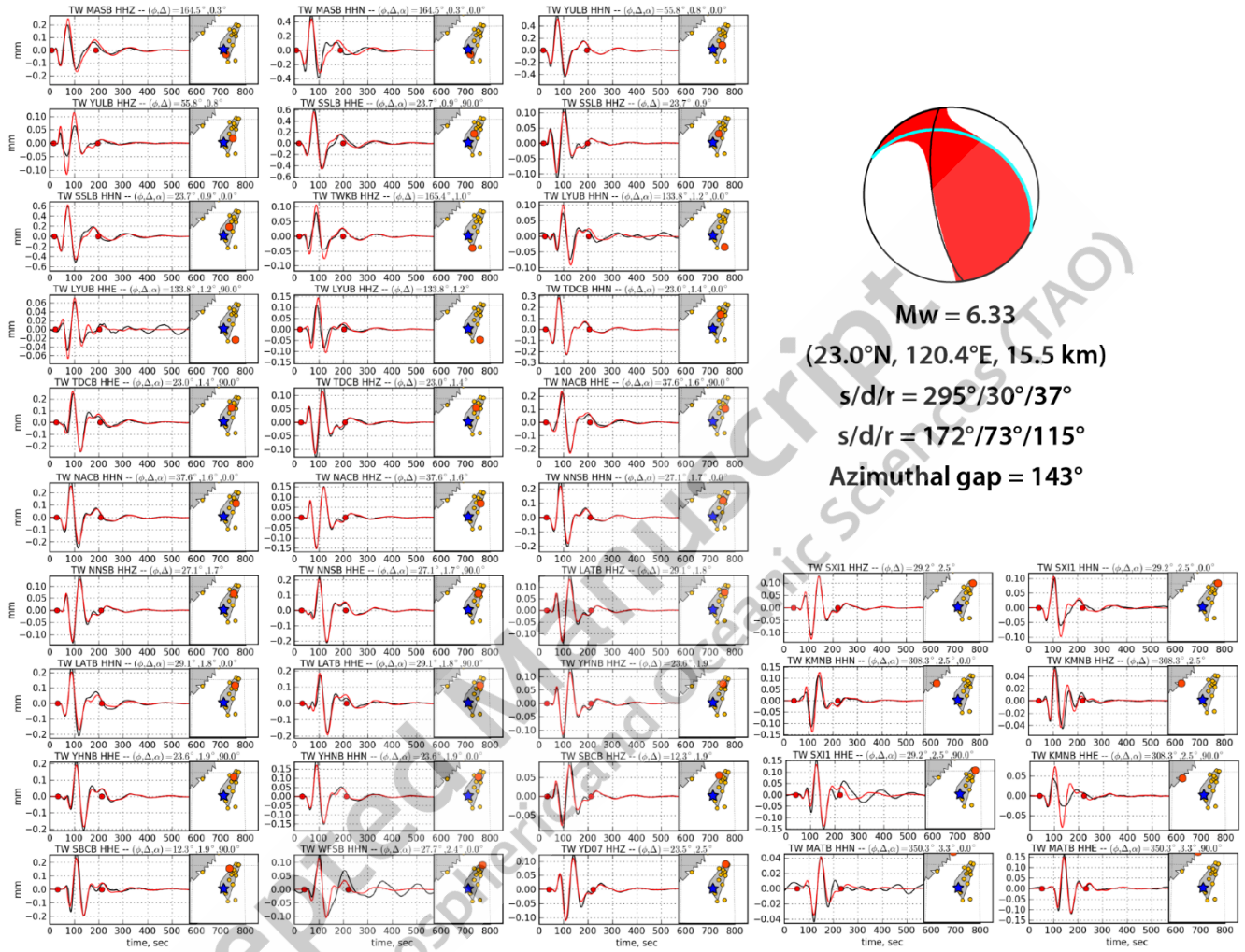

Figure 3.

Inversion of W phases at the frequency band of 0.0067 Hz (150 s) to 0.02 Hz (50 s). The black and red curves show the observed and synthetic waveforms computed for the solution shown. The two red dots bracket the portion of the observed waveforms used for inversion.

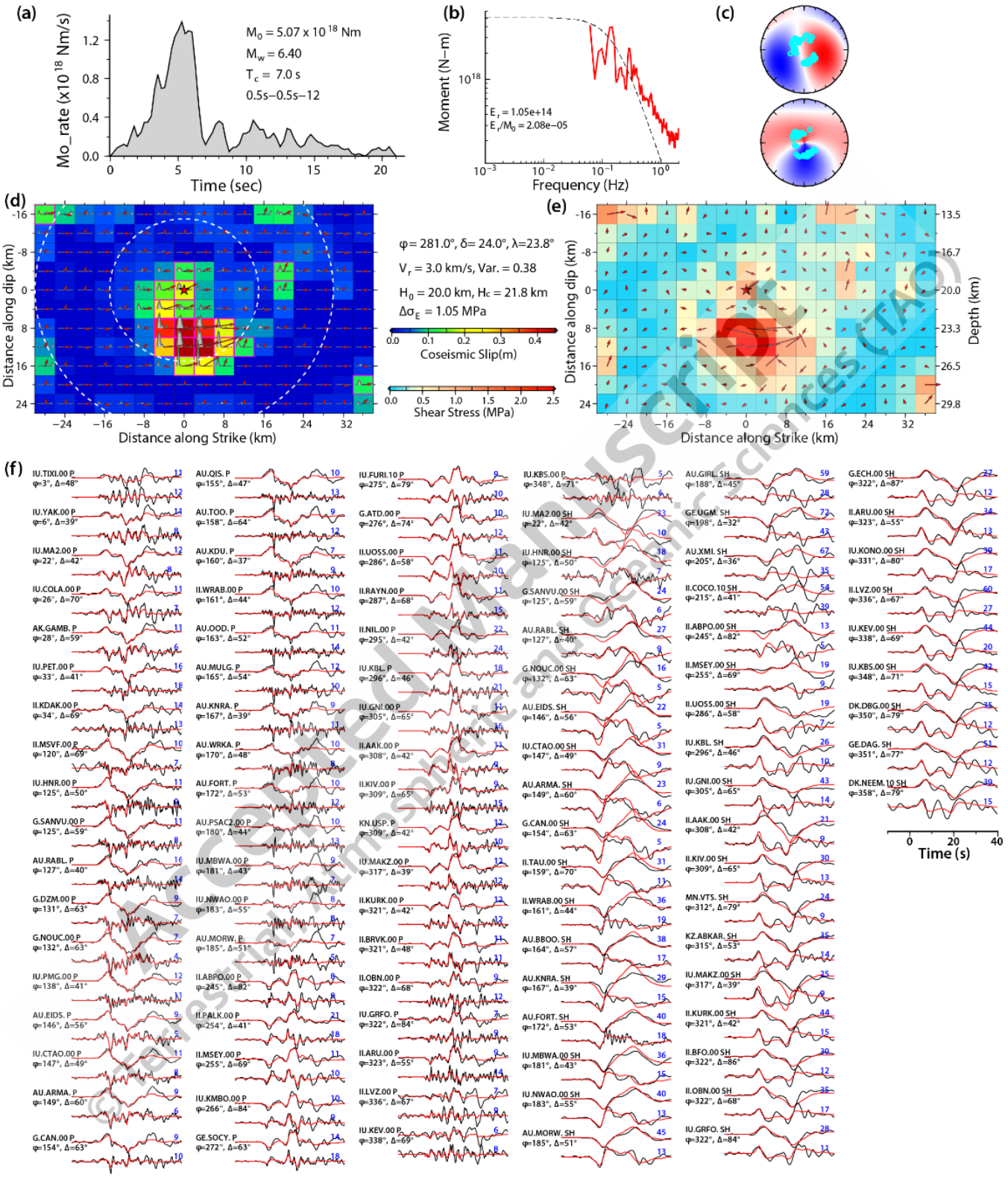

Figure 4.

Inversion of teleseismic body waves. a) Moment-rate function and b) moment-rate spectrum. c) P and SH radiation patterns with the stations used for inversion. The mechanism is given by (slip/dip/rake=281°/24°/24°), d) Slip distribution, e) distribution of stress drop, and f) observed (black) and computed (red) teleseismic P and SH displacement and velocity waveforms. For each station, the first row shows the displacement and the second row shows the velocity. A rupture speed of 3 km/s is assumed.

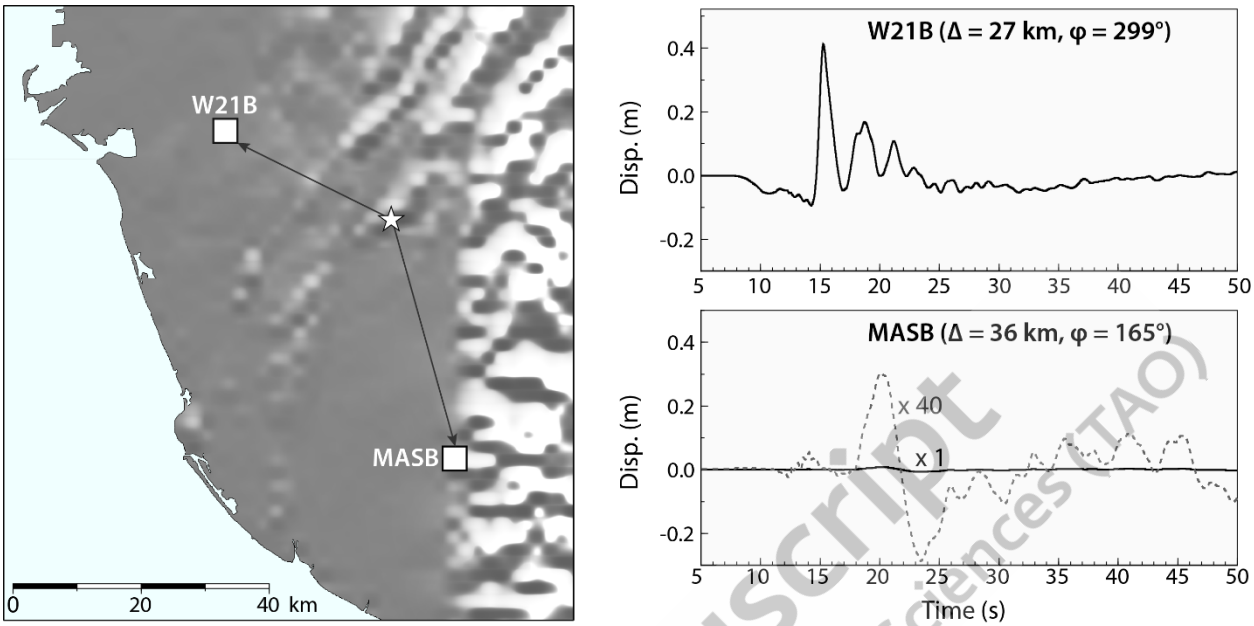

Figure 5.

Comparison of the EW component displacement waveforms at the stations W21B and MASB. On the plot for MASB, the black curve (marked as x1) is the plot with the same amplitude scale as that for W21B, and the gray curve (x40) shows the displacement multiplied by 40, indicating that the trace amplitude at W21B is about 35 times larger than that at MASB.

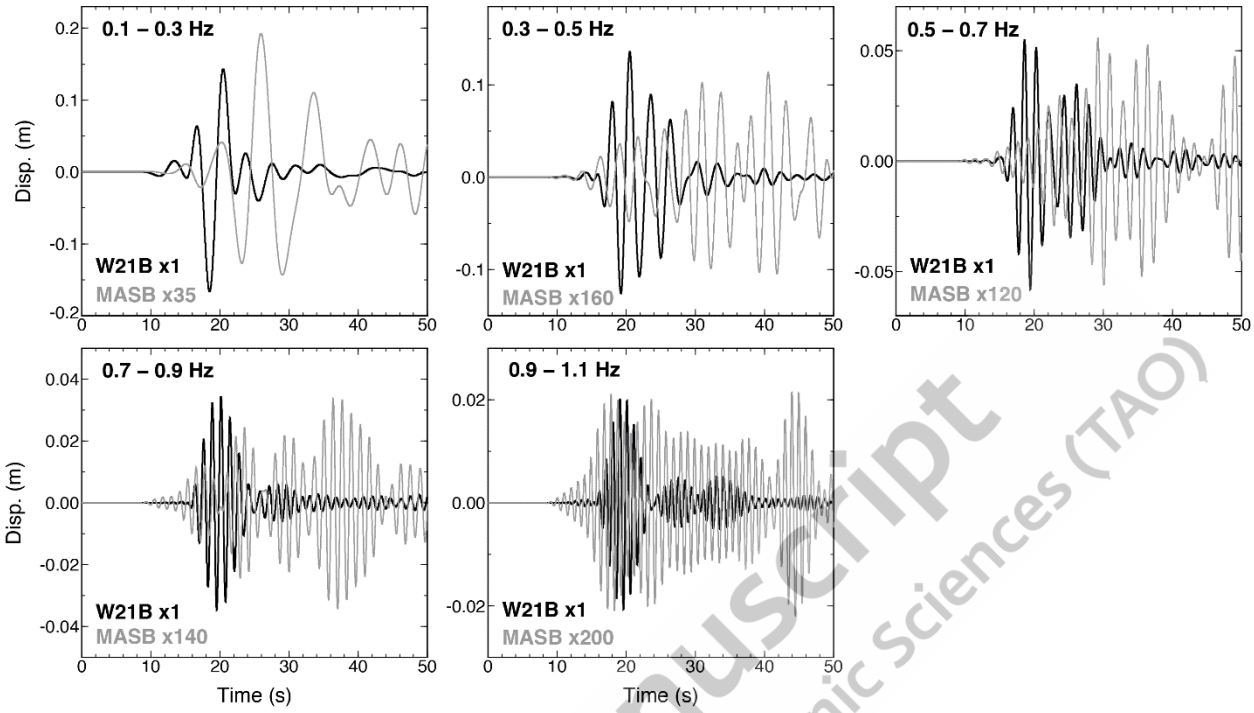

Figure 6.

Comparison of the amplitude at W21B (black) and at MASB (gray) at 5 frequency bands. For each frequency band the records are Butterworth band-pass filtered. For comparison, the MASB record is multiplied by a factor given at the lower left of each figure. Note that at the frequency band 0.3 to 0.5 Hz (2 to 3.3 s), the amplitude ratio is about 160.

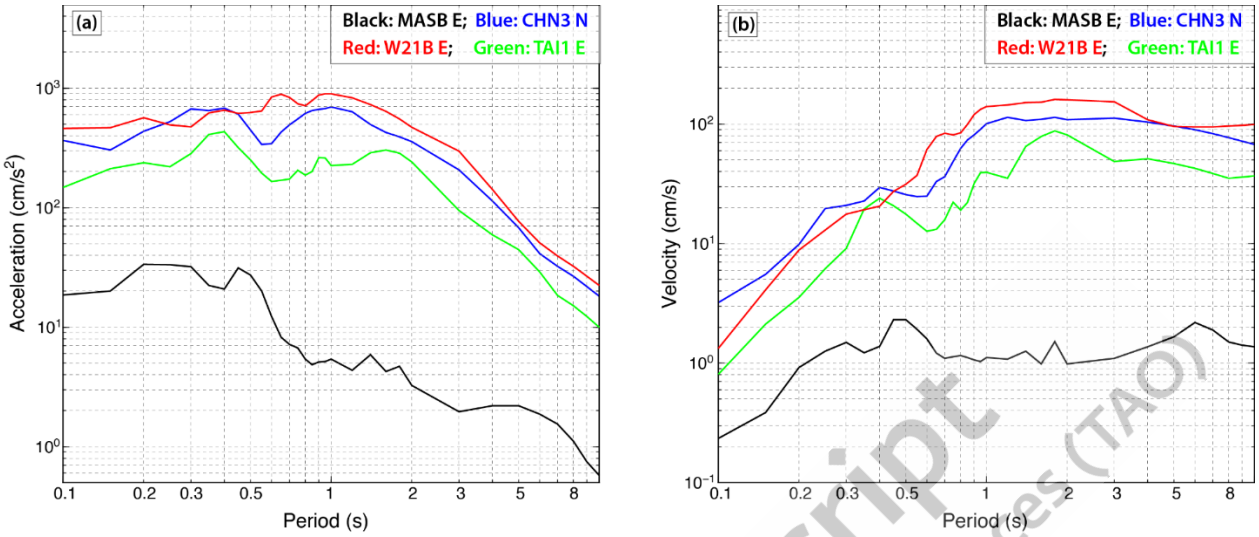

Figure 7.

Spectral acceleration (a) and spectral velocity (b) computed for the records at MASB (EW component), W21B (EW component), CHN3 (NS component), and TAI1 (EW component). Damping is 5 %.

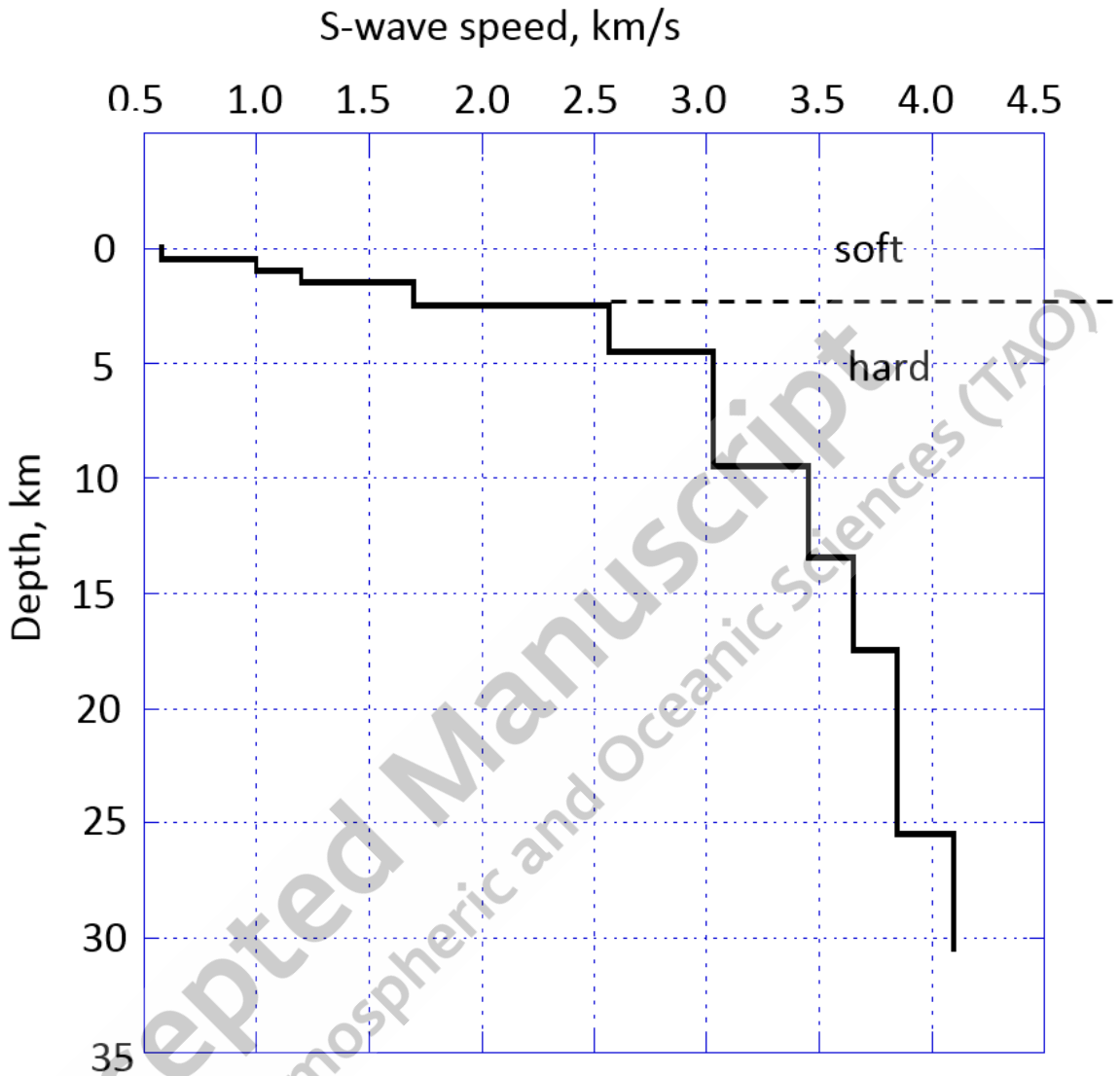

Figure 8.

S-wave vertical profile used for the "soft" structure model. The "hard structure model is obtained by removing the top 5 layers above the depth indicated by a dashed line.

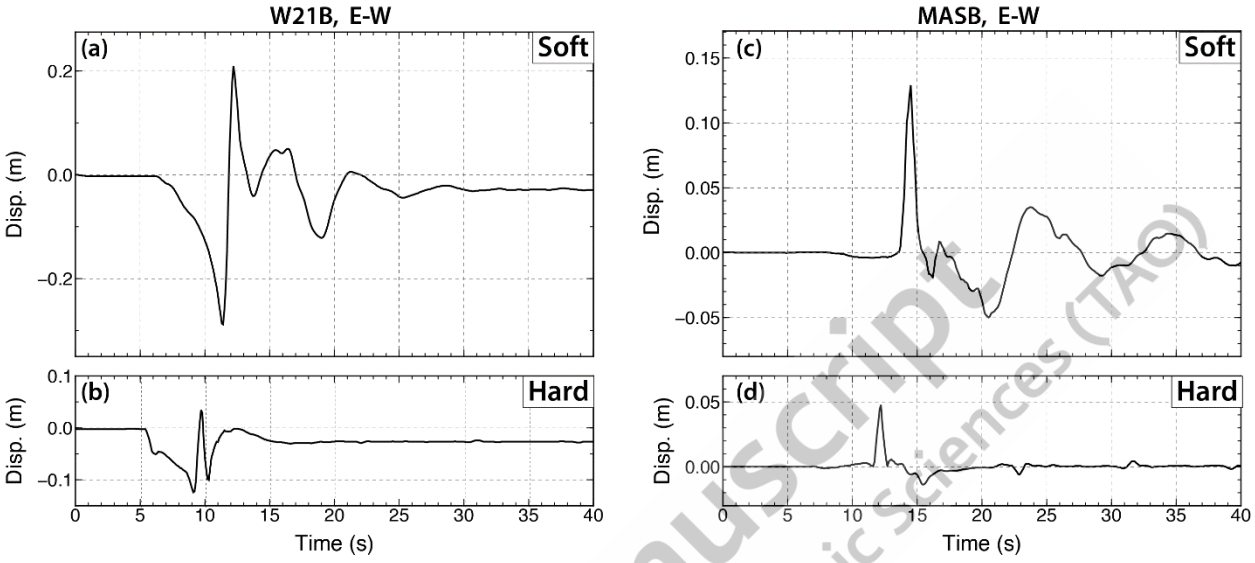

Figure 9.

Synthetic displacement waveforms computed for the stations W21B and MASB using the "soft" and "hard" structure models.

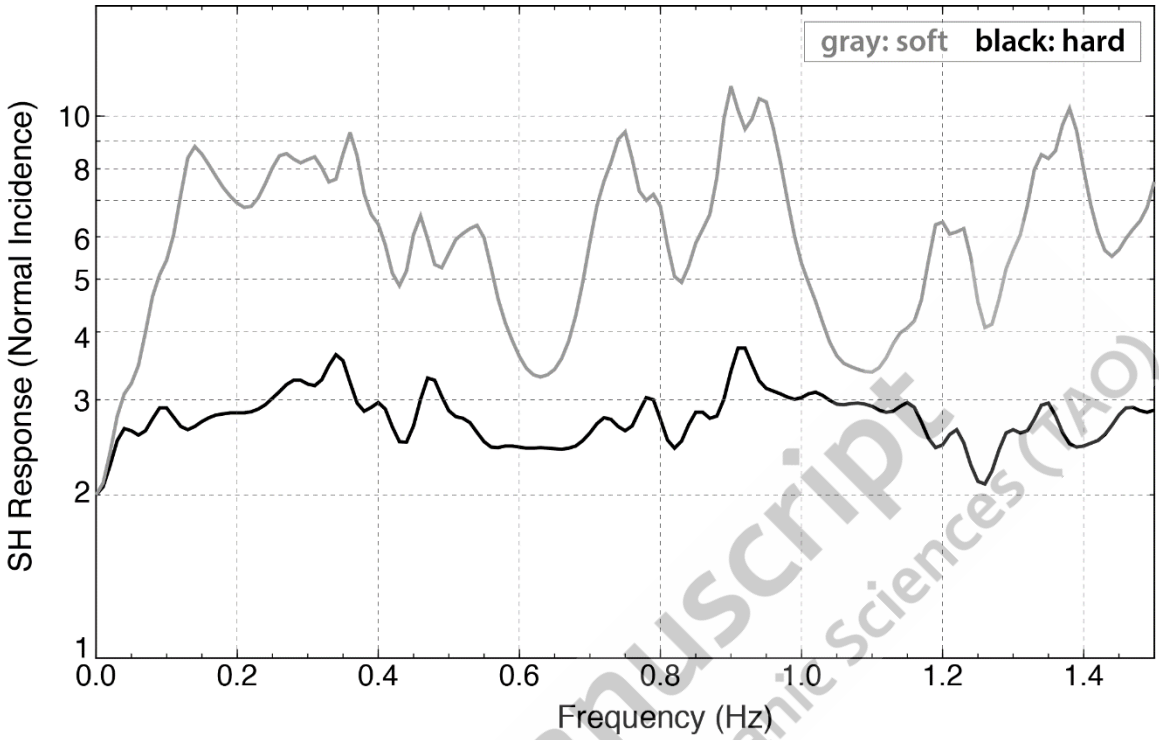

Figure 10.

Crustal response functions for a vertically incident plane SH waves for the “soft” (gray curve) and “hard” (black curve) crustal structure models.

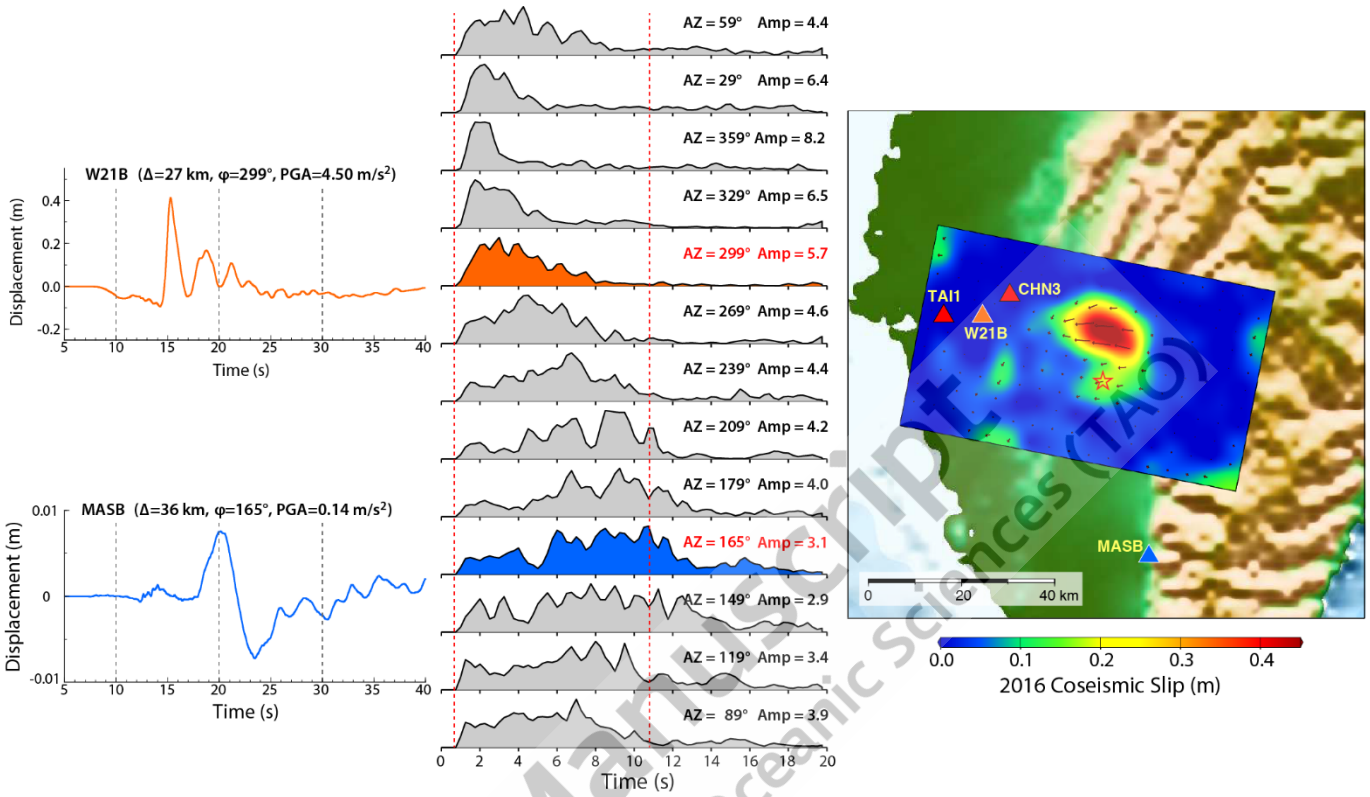

Figure 11.

The moment-rate functions (shaded pattern) viewed from various azimuths. The slip distribution is shown on the right. The stations W21B and MASB are located in the azimuth of 299° and 165. The moment-rate functions viewed from the azimuth of W21B and MASB are shown in red and blue, respectively. The displacement record at the respective station is shown for comparison.

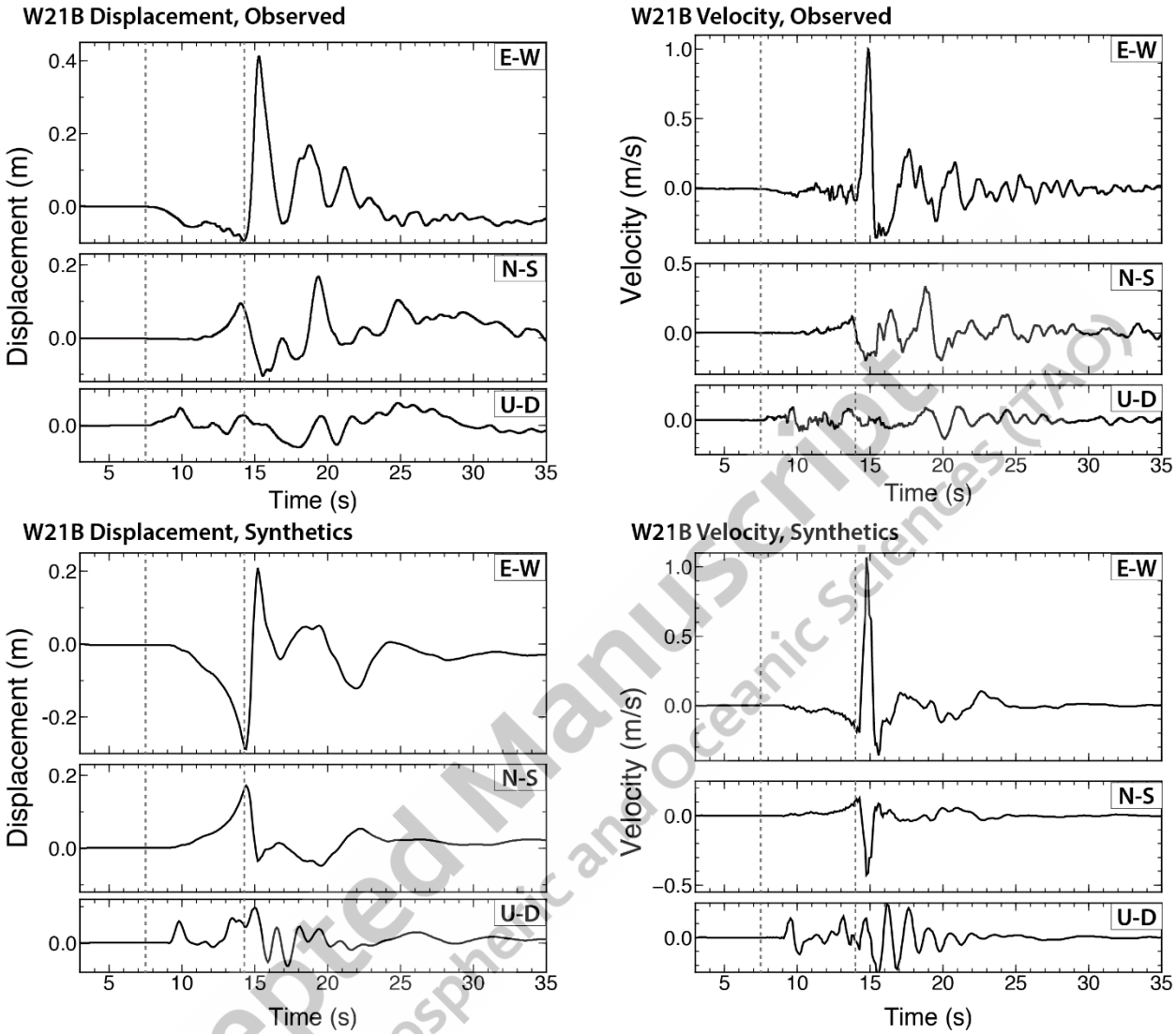

Figure 12a

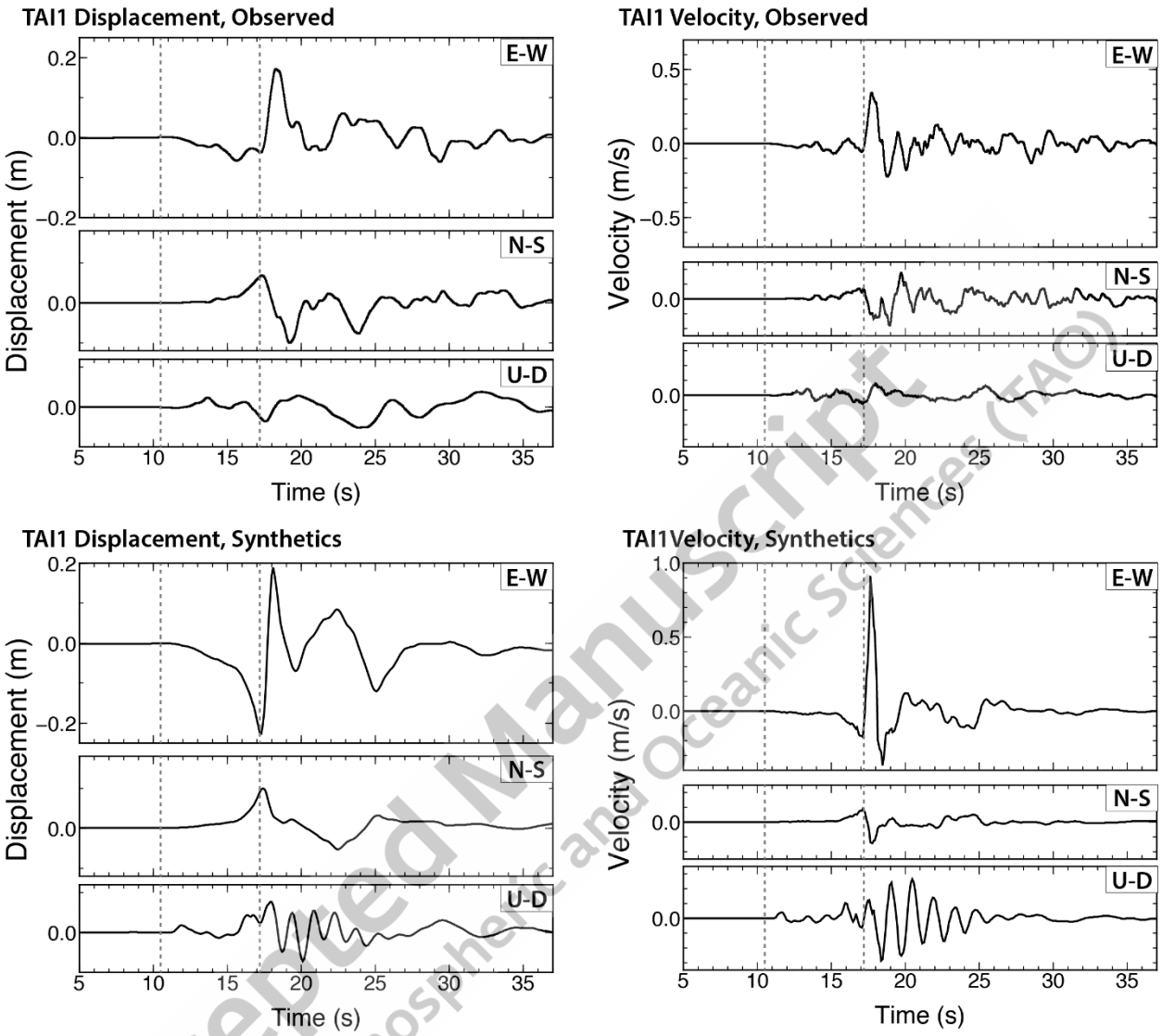

Figure 12b.

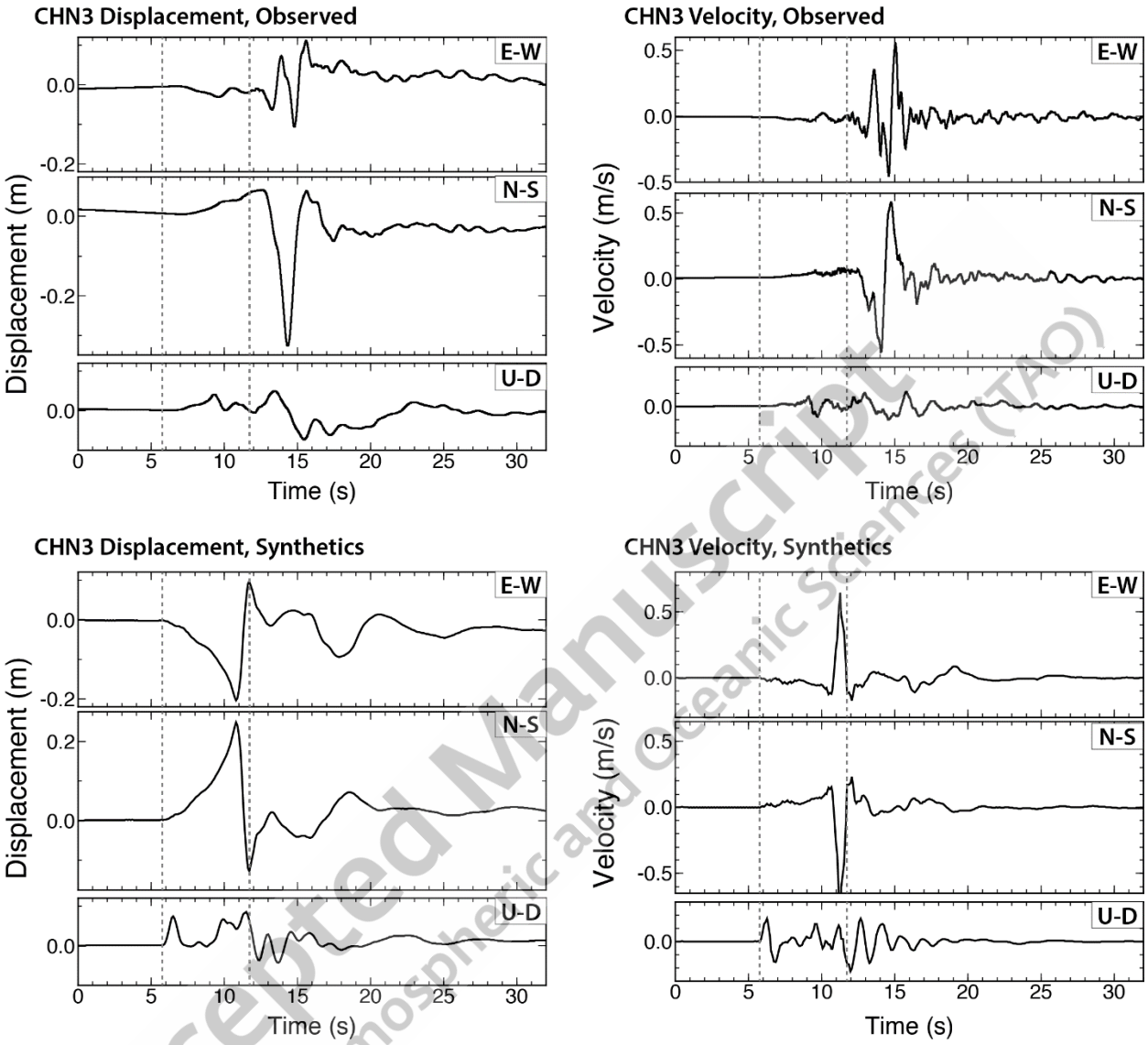

Figure 12.

Comparison of the observed (top) and synthetic (bottom) waveforms for the station W21B (Figure 12a), TAI1 (Figure 12b), and CHN3 (Figure 12c). Three-component displacement and velocity waveforms are shown. The "soft" crustal structure model is used.

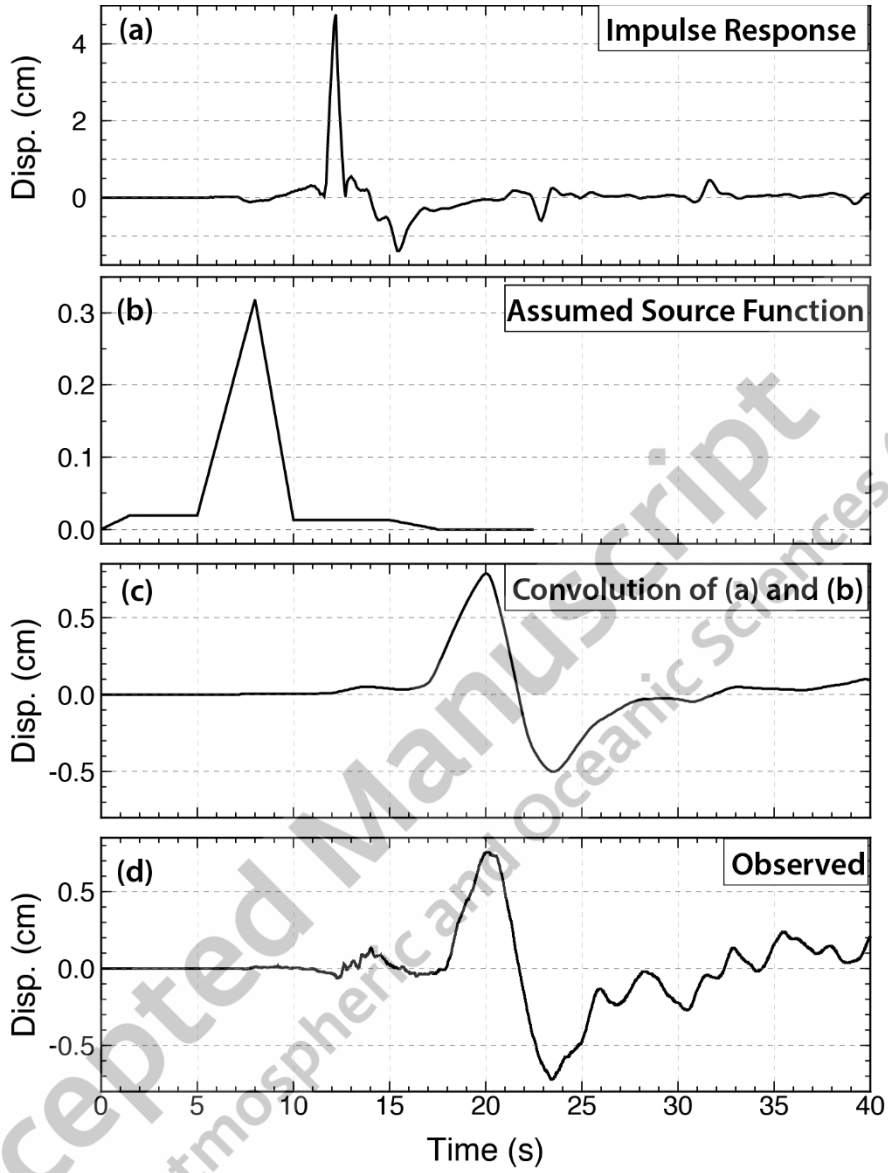

Figure 13.

Comparison of the observed and synthetic E-W component waveforms for the station MASB. The "hard" crustal structure model is used. a) Synthetic displacement waveform computed for a trapezoidal source function with a total duration of 0.3 s. b) The assumed moment-rate function. c) Convolution of a) and b). d) The observed displacement waveform.

